Tellus (1994), 46A, 433–447
Printed in Belgium – all rights reserved

TELLUS
ISSN 0280–6495

Simulation and hindcasts of tropical Pacific Ocean interannual variability

By MICHAEL K. DAVEY[1]*, SARAH INESON[1] and MAGDALENA A. BALMASEDA[2], [1]*Hadley Centre, Meteorological Office, London Road, Bracknell RG12 2SY, UK*; [2]*Atmospheric, Oceanic and Planetary Physics, Clarendon Laboratory, Parks Road, Oxford OX1 3PU, UK*

(Manuscript received 9 August 1993; in final form 24 February 1994)

ABSTRACT

A general circulation model of the tropical Pacific Ocean with a high resolution equatorial region is forced with observed winds from 1961 to 1993 to obtain a simulation of oceanic variability. Observed interannual sea surface temperature anomalies are reproduced well in the central equatorial Pacific, which is a region of strong variations in air–sea interaction. Combined principal oscillation pattern analysis of SST, heat content and zonal wind stress anomalies leads to a dominant interannual mode with a period of about 3 years. An empirical atmosphere model is constructed using the observed wind stress and the dominant simulated SST anomaly patterns. With the OGCM coupled to this statistical atmosphere, several hindcasts are made for the main recent ENSO events. Cold events are reproduced reasonably well, warm events less well: in particular, the 1982/83 hindcasts failed to produce a warming.

1. Introduction

The largest interannual variations in climate occur in the tropical Pacific region, and are associated with strong interaction between the atmosphere and ocean. These variations have widespread effects (see, e.g., Glantz et al., 1991), and in recent years there has been an intense observational and modelling effort aimed at understanding and predicting such changes. To a large extent, the atmospheric climate in the tropics is determined by the sea surface temperature (SST), so most prediction efforts focus on determining changes in SST. Several statistical (e.g., Barnett et al., 1988; Xu and von Storch, 1990) and dynamical (e.g., Cane et al., 1986; Latif et al., 1993c) models show predictive skill at lead times of up to a year: see the review by Latif et al. (1993a). The first successful dynamical model (Cane and Zebiak, 1985) used a reduced physics ocean coupled to a similarly simplified equilibrium atmosphere. The success of such a model stems from its ability to follow the evolution of the ocean after forcing it with observed winds: coupling to an atmosphere is necessary on seasonal timescales because SST changes drive surface wind changes that in turn alter the ocean state significantly.

With the advent of increased computer power, prediction experiments using general circulation models (GCMs) with a comprehensive range of physics have become feasible: Latif et al. (1993b) and Miyakoda et al. (1993) describe hindcasts using coupled ocean and atmosphere GCMs. Although one would expect coupled GCMs to provide the best predictions, relatively few coupled GCM hindcasts have been tried to date and there is as yet no clear evidence that they are better. An atmospheric GCM need not be used from the outset to determine atmospheric changes in detail: such changes could be found by forcing an atmospheric GCM with predicted SST anomalies corrected for known model errors (see Bengtsson et al., 1993).

In this study, we concentrate on seasonal changes in SST. The tropical Pacific ocean GCM

* Corresponding author.

(Section 2) is forced by observed winds to obtain a simulation of ocean variability from 1961 to 1993 (Section 3). The prediction strategy is to use an ocean GCM coupled to a simple statistical surface wind stress model (Section 4): the method is similar, but not identical, to that described by Barnett et al. (1993). Results from a limited set of hindcasts of recent ENSO events are described in Section 5.

2. Ocean model description

A Bryan/Cox type of ocean general circulation model (Cox, 1984) is used with a variable finite difference spatial grid. In the meridional direction grid spacing is 1/3° around the equator, increasing poleward to 1° at the open boundaries at 30° North and South. Zonally the spacing is 1.5° over most of the ocean, decreasing to 0.5° near the closed eastern and western boundaries. There are 16 levels in the vertical, at 5, 15, 25, 35, 48, 67, 96, 139, 204, 301, 447, 666, 996, 1490, 2232 and 3339 m.

The barotropic mode is omitted because barotropic currents are very small in the tropics. There is no variation in model bottom topography. The horizontal eddy viscosity decreases as grid spacing decreases, with a minimum value of 2×10^3 $m^2 s^{-1}$. Eddy diffusivity for temperature and salinity is constant at $2 \times 10^3 m^2 s^{-1}$ over most of the domain, increasing to $3 \times 10^4 m^2 s^{-1}$ near the open northern and southern boundaries. Temperature and salinity at these open boundaries are kept close to their seasonally varying climatological values taken from the Levitus (1982) climatology. Short-wave radiation is allowed to penetrate below the top model layer, attenuated using a two-band approximation. Two types of vertical mixing are used. Richardson number dependent diffusivity (Pacanowski and Philander, 1981) is applied with $\nu_b = 0.5 \times 10^{-4} m^2 s^{-1}$, $\kappa_b = 0.05 \times 10^{-4} m^2 s^{-1}$, and $\nu_0 = 55 \times 10^{-4} m^2 s^{-1}$. A Kraus/Turner mixing scheme (Kraus and Turner, 1967) is also embedded in this model, principally to represent surface-generated turbulence, with wind energy related to the Hellerman and Rosenstein (1983) seasonal climatology. Apart from the addition of the Kraus/Turner mixing, the basic model configuration is essentially that used by Gordon and Corry (1991), wherein further details may be found. Gordon and Corry described the seasonal cycle of the model when forced by climatological and atmospheric model fluxes: in this paper different forcing fields are used (see below), and attention is focussed on interannual variability.

The model was first spun up using monthly climatological fields. The Hellerman and Rosenstein wind stress was used, reduced by a factor of 0.75 to take into account the overestimate of tropical stresses. Surface heat flux Q is calculated as

$$Q = Q_0 - (dQ/dT)_0 (T_0 - T), \tag{1}$$

where T is model SST, Q_0 and T_0 are monthly climatological heat flux and SST, and $(dQ/dT)_0$ (which is negative) is an estimate of the dependence of Q on changes in SST. Climatological values are taken from Oberhuber (1988). Salinity S is controlled either by using observed fresh water fluxes F_0 ($kg\,m^{-2}\,s^{-1}$), or by forcing surface salinities toward observed values using

$$F = F_0 + \lambda(S_0 - S). \tag{2}$$

Here, F_0 is the climatological net surface fresh water flux (evaporation from Esbensen and Kushnir (1981); precipitation from Jaeger (1976)), S_0 is the climatological salinity (Levitus, 1982), and $\lambda = (35\,Wm^{-2}\,K^{-1})/(S_{00} c_p)$, where c_p is specific heat and $S_{00} = 0.035$ is a standard salinity value.

The seasonal cycle thus obtained, using fresh water flux $F = F_0$, is described in detail in Stockdale et al. (1993), where the behaviour of seven tropical Pacific ocean general circulation models with the same wind and thermal forcing is intercompared. The main observed circulation features are simulated quite well. With regard to SST, the main defects (in common with other models considered in the intercomparison) are that the west Pacific is slightly too warm, and the equatorial cold tongue in the central east Pacific is too cold (by about 1°C on average).

3. Simulated interannual variability

The ocean model was forced using the Florida State University (FSU) analysis of observed winds (Goldenberg and O'Brien, 1981). This dataset

has been used for multi-year Pacific Ocean simulations with a variety of models: see for example Busalacchi et al. (1983), Kubota and O'Brien (1988), Zebiak (1989) (models without thermodynamics); Seager (1989) and Wakata and Sarachik (1991) (simplified models with thermodynamics). Miller et al. (1993) compare in detail simulations made using the Zebiak and Cane (1987) simplified ocean and three OGCMs of different types, including a variation of the Cox/Bryan type considered here.

For the present model a drag coefficient of $0.75 \times 1.535 \times 10^{-3}$ and an air density of $1.2\,\mathrm{kg\,m^{-3}}$ were chosen: the factor of 1.535 gives average stress values that are close to the Hellerman/Rosenstein climatology (Stockdale, 1992). A seasonal cycle was first established using the 1966–1985 average of the FSU winds, with heat and fresh water fluxes (1) and (2). The seasonal cycle in SST thus obtained was very similar to that described in Stockdale et al. (1993).

The surface heat flux formulation was then modified to

$$Q = Q_0 - (\mathrm{d}Q/\mathrm{d}T)_0\,(T_0 - T_\mathrm{m}) - 0.3(\mathrm{d}Q/\mathrm{D}T)_0\,(T_\mathrm{m} - T), \qquad (3)$$

where T_m denotes the model SST seasonal cycle (interpolated in time from monthly averages). Thus, anomalies from the model seasonal cycle are weakly damped, with the factor 0.3 chosen such that model interannual SST anomalies have similar magnitude to those observed. The reduction in damping can be rationalised by considering the linearisation used by Oberhuber (1988) in estimating $\mathrm{d}Q/\mathrm{d}T$, which used fixed climatological

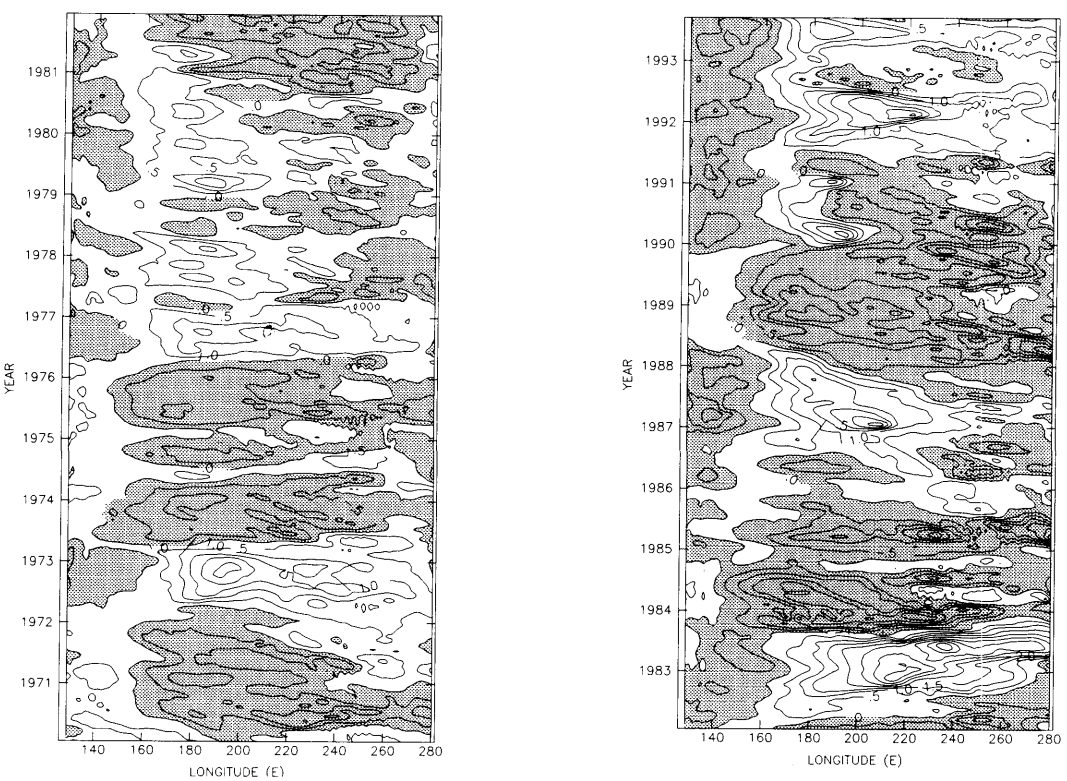

Fig. 1. Time-longitude sections of the simulated sea surface temperature anomalies SST′ averaged from 5° N–5° S, for 1970 to 1993. Anomalies shown are departures from the model monthly climatology calculated from the 1966–1990 simulation period. Contour interval 0.5 °C, negative values shaded. Time labels indicate the beginning of the respective years.

air temperatures: if changes in air temperature are allowed in response to SST anomalies then dQ/dT is reduced. (For further discussion see Stockdale (1992). Lower values of dQ/dT are also advocated by Wells and King-Hele (1990).) The fresh water flux (2) was unchanged.

Winds from 1961 to 1993 were used, with no detrending. In the first 5 years, the agreement of SST with observations is relatively poor, probably because the winds are less reliable at that time and contain a distinct trend. Thus, results are presented from 1966 onwards. Model monthly climatological fields are defined by taking averages from the years 1966 to 1990 (inclusive), and interannual anomalies (denoted by ′) are perturbations from those means. Fig. 1 shows model SST′ in the equatorial band (5°N–5°S) for 1970–1993: the main warm El Niño (1972/73, 82/83, 86/87, 91/92/93) and cold La Niña events are prominent. During the large 1982/83 event the warm model SST anomalies first appear in the west Pacific, and then intensify and rapidly extend eastward across the central and east Pacific. Observed behaviour was similar, but with less pronounced eastward movement and with warming more concentrated in the east Pacific. While eastward spread of warm SST′ is evident during the large 1982/83 event, at other times there is less movement, with a weak tendency for westward spread in the central Pacific. The magnitude of variability is comparable to that observed, but the spatial distribution of model interannual variability (not shown) reveals largest amplitude confined close to the equator, peaking in the central Pacific, whereas observed interannual variability is less equatorially concentrated and is largest in the east Pacific.

The spatial distribution in Fig. 2 of the correlation r of timeseries of simulated and observed SST′ (observed values from the UKMO Global Ice and Sea Surface Temperature (GISST) dataset) shows that the pattern of evolution is best (r up to 0.8) in the central equatorial Pacific, good near the South American coast south of the equator (up to 0.6), and poor in the western Pacific and away from the equator. Other OGCMs similarly have highest correlations in the central equatorial Pacific (see Fig. 4 in Miller et al. (1993)). Rms errors (not shown) are largest in the east-central equatorial region where SST is most variable. Timeseries of observed and simulated SST anomalies averaged over the so-called Niño3 region (5°N–5°S, 150°W–90°W) are given in Fig. 3: the amplitude as well as the shape of the anomalies is reasonably well reproduced by the model. In this region the main poor features are the underestimation of the 1986/87 warming, and the spurious cool event in 1989/90. 2 sharp false cool episodes occur in December 1983 and March 1985: these also appear in other simulations (see, Fig. 1b of Miller et al. (1993)), and are due to unusually strong easterlies in the FSU dataset in the preceding months. A delay in the peak of the 1982/83 event also appears in most other simulations, an exception being the Zebiak and Cane (1987) model. The 1991/92 warm event is well simulated, but the recurrence in 1993 is weaker than observed.

Heat content (HC) of the upper ocean was calculated as the depth average of temperatures for the top 10 model levels (to 360 m depth). Time-longitude diagrams of HC′ have features that are similar to those described by Chao and Philander (1993) for a similar simulation. There is

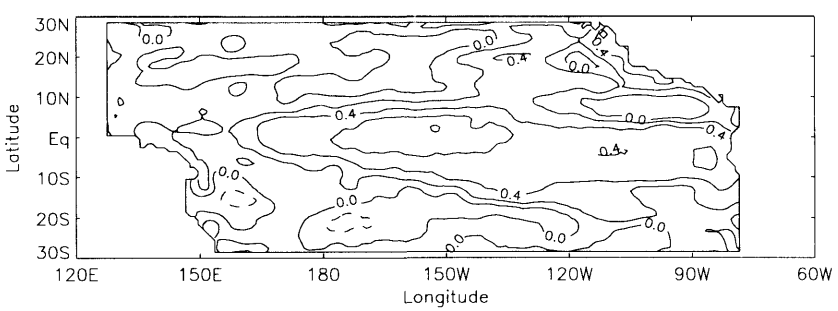

Fig. 2. Correlation of observed (UKMO GISST dataset) and simulated sea surface temperature anomalies SST′ calculated on a 1° × 1° latitude-longitude grid. Model anomalies are departures from monthly climatology calculated from the 1966–1990 simulation period. Contour interval 0.2, negative contours dashed.

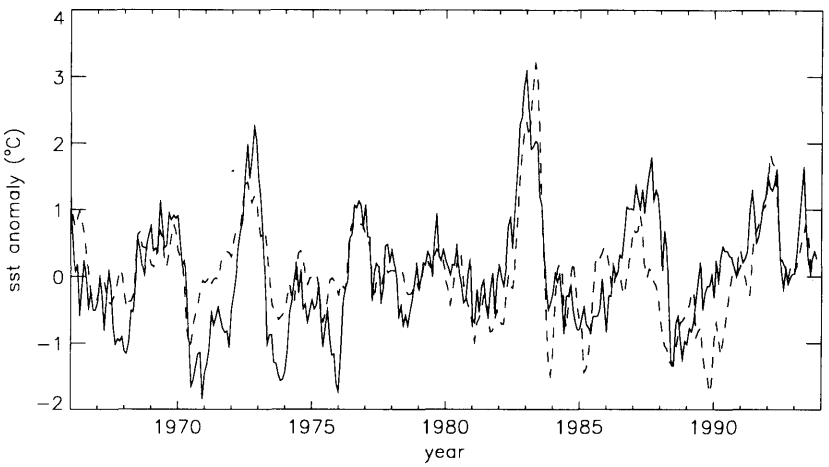

Fig. 3. Time series of monthly observed (solid) and simulated (dashed) sea surface temperature anomalies SST′ in region Niño3 (5°N–5°S, 150°W–90°W).

generally eastward propagation along most of the equator (in contrast to the more stationary SST anomalies), with slow (0.2 to 0.3 m s^{-1}) movement in the west to about 160°W, followed by a rapid spread (0.8 to 1.9 m s^{-1}) to the east coast. In sections at 8.5° off the equator there is slow westward propagation, with largest anomalies in the west Pacific: near the western boundary these then move equatorward and continue as eastward propagating anomalies along the equator.

A principal oscillation pattern (POP) analysis (Hasselman, 1988; Von Storch et al., 1993) of combined SST′, HC′ and zonal wind stress TAUX′ was carried out. The different fields were separately normalised by their standard deviations (0.55°C, 0.44°C, 0.019 N m^{-2} respectively), then empirical orthogonal functions (EOFs) of the combined fields were obtained, ranked in order of decreasing explained variance. POP analysis was applied to the timeseries of EOF coefficients, for K (up to 20) EOFs, to obtain oscillating (complex pairs) and decaying modes. Let $F(\boldsymbol{x}_m, t_n)$ denote the combined field at M spatial points $\boldsymbol{x}_m$ and N timepoints t_n, as represented by K EOFs. Then, in terms of POP modes

$$F(\boldsymbol{x}_m, t_n) = \sum_{\text{osc}} [\text{pop}_R(\boldsymbol{x}_m)\,\Gamma_R\,T_R(t_n) + \text{pop}_I(\boldsymbol{x}_m)\,\Gamma_I\,T_I(t_n)] \sum_{\text{decay}} \text{pop}_D(\boldsymbol{x}_m)\,\Gamma_D\,T_D(t_n), \quad (4)$$

where pop_R and pop_I are the real and imaginary components of spatial patterns for oscillating modes; pop_D denotes the pattern of a decaying mode; and T_R, T_I and T_D denote corresponding time series of the amplitudes of the patterns. The time series and spatial patterns are normalised: in particular,

$$\sum_m \text{pop}_R^2(\boldsymbol{x}_m) + \text{pop}_I^2(\boldsymbol{x}_m) = 1.$$

The constants Γ contain the scaling information. Further, real and imaginary pairs of the combined spatial patterns are chosen to be orthogonal. (Note however that patterns from different oscillating pairs are generally not orthogonal.)

From the POP analyses, the period of the ENSO-related oscillating mode was between 32 and 40 months (depending on the number of EOFs used), with a decay timescale of 12 to 20 months. The main features described below, obtained with 5 EOFs, are common to all the analyses. (The first 5 EOFs explain 30.7, 8.8, 5.9, 3.7 and 3.2% of the total variance of the combined fields.)

Fig. 4 shows timeseries T_R and T_I for the ENSO-related mode, and corresponding spatial patterns are in Fig. 5. In this case, the imaginary mode pop_I corresponds to the warm peak of the ENSO cycle, and the real mode pop_R represents conditions at the transition between warm and

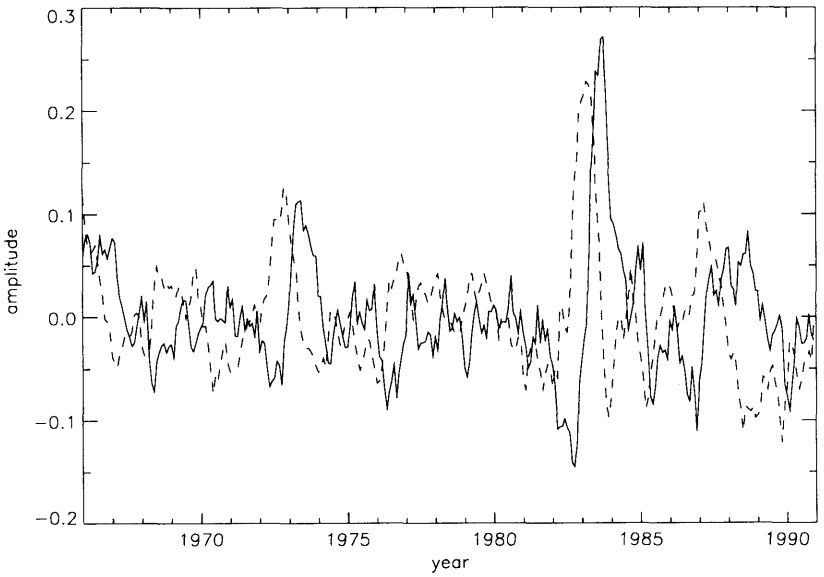

Fig. 4. Time series of the real (solid) and imaginary (dashed) components of the ENSO-related POP mode, obtained using five principal component timeseries for combined SST′/HC′/TAUX′ fields from the 1966–1990 simulation. The imaginary component is largest during peaks of ENSO events, while the real component is associated with ENSO transition.

cold peaks. Note that when the POP mode is freely oscillating the patterns appear in the sequence

$$\text{pop}_I \rightarrow \text{pop}_R \rightarrow -\text{pop}_I \rightarrow -\text{pop}_R \cdots . \qquad (5)$$

From the time series, we see that magnitude is relatively large during the main ENSO events, and that patterns then follow the sequence (5). At other times, magnitude is small and phase is not as clearly ordered.

The spatial patterns show similar features to those found by Latif et al. (1993a, b) from Pacific observations and simulations. (Note: the patterns shown here have been multiplied by the scales Γ_R and Γ_I to demonstrate their relative maximum amplitudes.) For SST′ the peak pattern, SST_I is large and positive in the equatorial central and east Pacific, while the transition pattern SST_R is relatively weak and has a zonally banded structure (negative on the equator, positive either side). As pointed out by Latif et al. (1993b), the meridional gradients in SST_R may be effective in forcing anomalous winds. Overall, SST′ appears as a standing oscillation.

The HC′ patterns are much less equatorially confined than their SST′ counterparts. The peak HC′ pattern HC_I has strong zonal contrast, positive in the east and negative in the west Pacific. The central-eastern lobe is largest along the equator and the American coasts, while in the west there are maxima off the equator. The transition HC_R shows a negative band all along the equator, still with off equatorial maxima in the west Pacific with similar magnitude to HC_I. Bearing in mind sequence (5), this represents propagation from west to east along the equator. The positive areas along the American coast in HC_I now appear in HC_R as weak anomalies offshore.

In $TAUX_I$, the main peak feature is a patch of westerlies on the equator, located to the west of the warm equatorial anomaly in SST_I, and, still further west, weaker easterlies about 15° either side of the equator. The transition pattern $TAUX_R$ has weak winds on the equator, and west Pacific off-equatorial features similar to $TAUX_I$. With the inclusion of more EOFs in the POP analysis, these off-equatorial features strengthen and extend further eastward across the Pacific.

The overall picture is, for example, of a build up of negative HC′ in the west Pacific during a warm El Niño phase when TAUX′ is westerly on the equator with easterly off-equatorial bands;

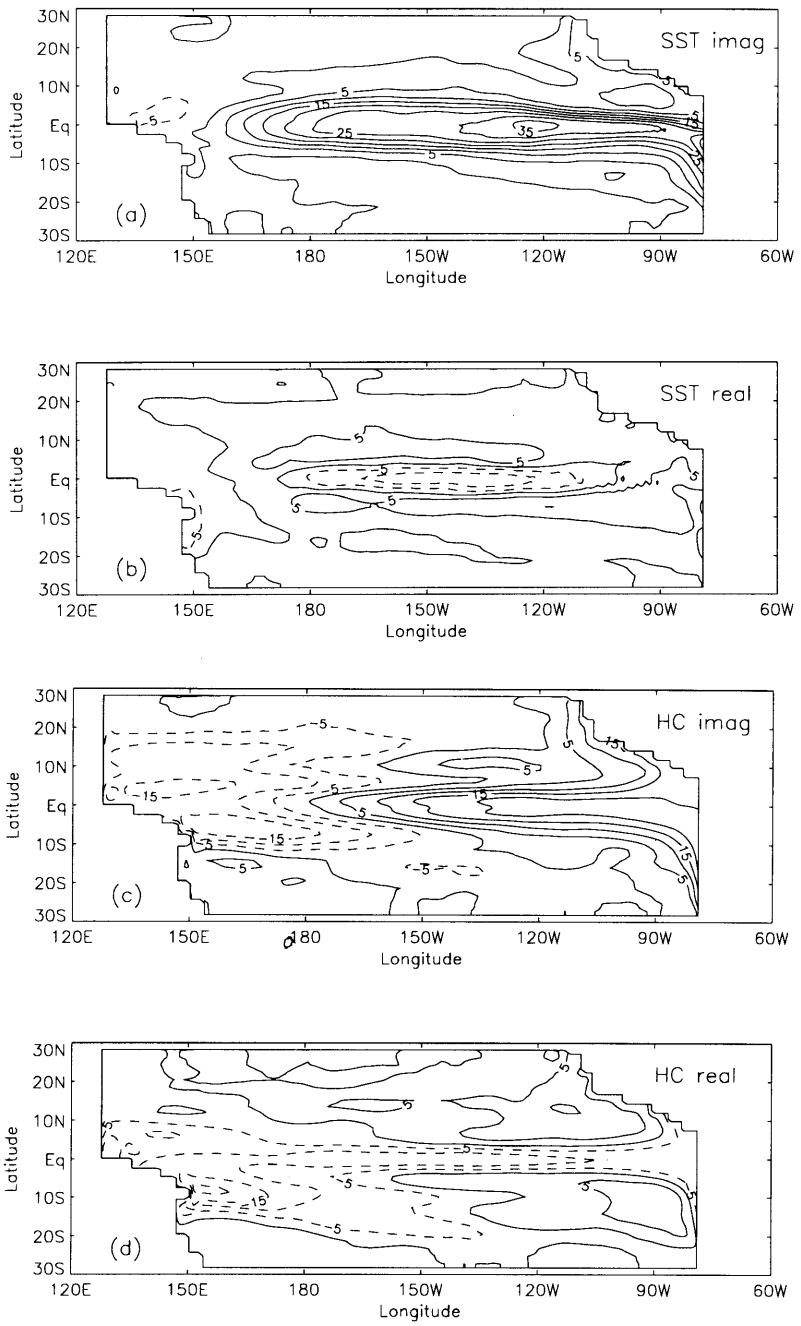

Fig. 5. Spatial patterns of the ENSO-related POP mode obtained using five EOFs and principal component timeseries for combined SST′/HC′/TAUX′ fields from the 1966–1990 simulation. SST_I, HC_I and $TAUX_I$ (panels a, c, e) are associated with peak ENSO phase (warm as shown), while SST_R, HC_R and $TAUX_R$ (b, d, f) are associated with transition ENSO phase (warm-to-cold as shown). The patterns are components of the normalised combined patterns pop_R and pop_I, multiplied by scales $\Gamma_R = 1405$ and $\Gamma_I = 1434$. Negative contours are dashed.

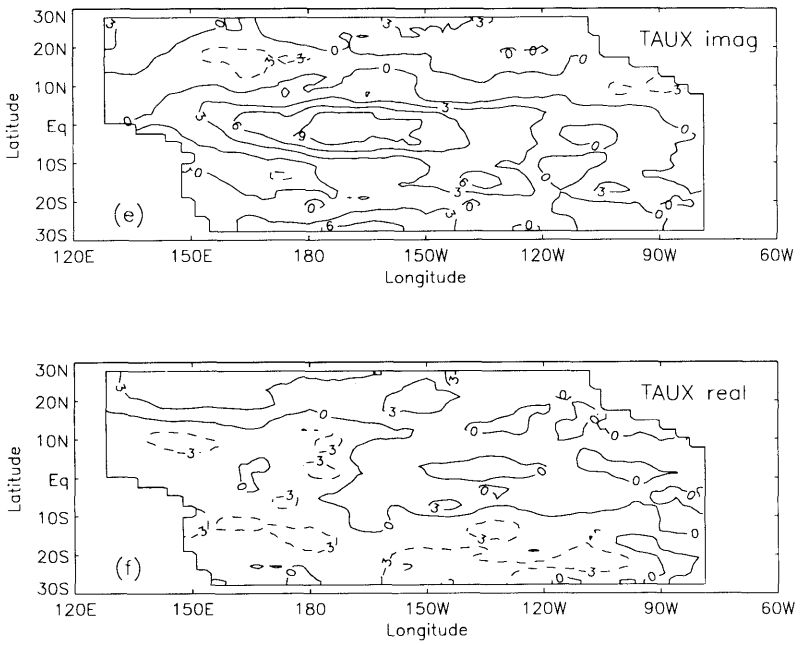

Fig. 5. Continued.

negative HC′ then expands eastward along the equator during the warm-to-cold transition, associated with a shallowing of the thermocline and consequent cooling of SST′ in the central-eastern Pacific. This cooling decreases the equatorial westerly TAUX′, which aids shallowing of the thermocline. Continued cooling moves the system into a La Niña phase, with easterly TAUX′ that increases HC′ in the west, ready for transition to the next warm phase of the cycle. As pointed out in similar studies (Chao and Philander, 1993; Latif et al., 1993a, b), this cycle is basically like the delayed oscillator mechanism proposed by Suarez and Schopf (1988). Note that the cycle is far from regular in practise: it is likely that other ocean-atmosphere mechanisms (cf., the coupled GCM analyses by Philander et al., 1992; Latif et al., 1993a) are also important, either separately or acting to excite the above cycle during quiet periods.

4. The empirical atmosphere

Some method of estimating the surface stress for a given ocean state is needed to make forecasts using the above ocean model. A dynamical atmospheric model could be used, but general circulation models are computationally expensive and the parameterisations required for accurate simpler models are not straightforward. Here we apply a linear statistical method to find the stress anomalies associated with the main SST′ patterns, and then use those patterns to estimate the stress for any given SST′. As in Wu et al. (1994) and Balmaseda et al. (1994), model SST′ is directly related to the observed wind stress anomalies. The method is similar to that used by Barnett et al. (1993).

The SST anomalies from the simulation are first written as

$$\mathrm{SST}'(\boldsymbol{x}_m, t_n) = \sum_{k=1}^{N} \mathrm{eof}_k(\boldsymbol{x}_m)\, \lambda_k\, pc_k(t_n), \qquad (6)$$

where the eof_k are empirical orthonormal functions, the pc_k are orthonormal principal component timeseries, and the λ_k are constants containing variance information, decreasing as k increases. From the observed wind stress anomalies τ_0' used in the ocean simulation, the associated patterns W_k are calculated as

$$W_k(\boldsymbol{x}_m) = \sum_n \tau_0'(\boldsymbol{x}_m, t_n)\, pc_k(t_n). \qquad (7)$$

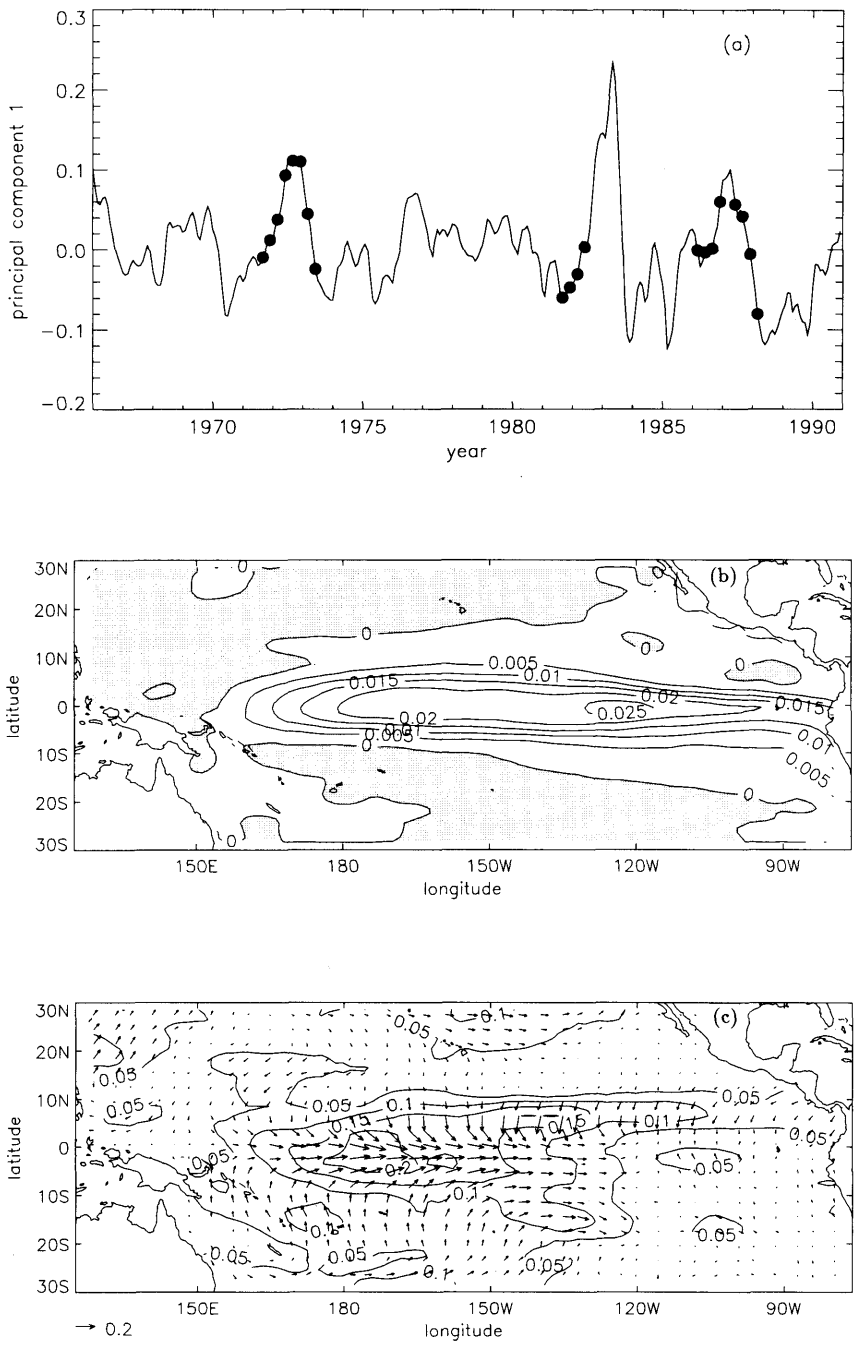

Fig. 6. EOF analysis of simulated SST′, and associated wind stress anomaly. (a) The principal component timeseries pc_1: solid circles indicate values for the month preceding each of 20 hindcasts for warm and cold ENSO events. (b) SST′ eof_1 "explains" 46.9% of the variance in the 1966–1990 simulation period. Negative values are shaded. (c) The associated wind stress anomaly pattern W_1. Contour interval 0.05 N m^{-2}.

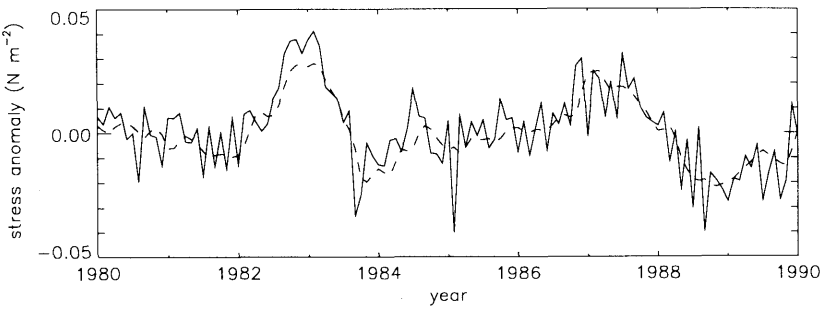

Fig. 7. Time series of zonal wind stress anomalies averaged over the region 5°N–5°S, 165°E–225°E, as used for the ocean simulation based on observed winds (solid), and as reconstructed using 5 SST′ EOFs and associated wind patterns (dashed).

The patterns eof_1, pc_1, and W_1 are shown in Fig. 6: from the timeseries pc_1 and the shape of eof_1 this is clearly an ENSO related pattern, resembling the peak POP pattern SST_1 in Fig. 5. The stresses for the simulation period can be reconstructed using the first K such patterns as

$$\tau'_r(\boldsymbol{x}_m, t_n) = \sum_{k=1}^{K} W_k(\boldsymbol{x}_m)\, pc_k(t_n). \tag{8}$$

The above procedure gives a best fit of reconstructed τ'_r to observed τ'_0 in the least squares sense. We will use $K=5$ patterns in the hindcasts described in the next section. (The first five EOFs for SST′ explain 46.9, 14.0, 6.1, 4.4 and 3.0% of the total variance.) The correlation of timeseries of observed and reconstructed zonal stress is best (r over 0.6) in the central equatorial region, generally about 0.4 in the equatorial region, but less than 0.2 poleward of 10°N or S. Fig. 7 shows timeseries of reconstructed and observed zonal wind stress averaged over the region 5°N–5°S, 165°E–225°E in the central Pacific for the 1980s: the reconstruction fits the observed pattern quite well. The 1982/83 peak is underestimated by about 30% however, when SST′ patterns were unusual.

At any time t, the stress anomaly for given SST′ is estimated by

$$\tau'(\boldsymbol{x}_m, t) = \sum_{k=1}^{5} W_k(\boldsymbol{x}_m)\, q_k(t), \tag{9}$$

where the predictors q_k are obtained by projecting SST′ onto the respective EOFs:

$$q_k(t) = \lambda_k^{-1} \sum_m \text{eof}_k(\boldsymbol{x}_m)\, \text{SST}'(\boldsymbol{x}_m, t). \tag{10}$$

During the simulation period this projection procedure simply reconstructs the principal component timeseries, so $q_k(t_n) = pc_k(t_n)$. Note that, in contrast to Barnett et al. (1993), no multiplicative factor is used to increase τ'_r further.

5. Hindcasts of ENSO events

Hindcasts were made by simply taking the ocean simulation state at the start date, and then continuing the integration, using the empirical atmosphere model to determine the wind stress anomalies every 3 days. No attempt is made to initialise the ocean state more accurately by using observed ocean data, so there is an initial ocean error due to the inaccuracies of the simulation. There is an initial jump (generally small) in the wind stress, due to the effective truncation of the stress reconstruction from that observed to that obtained using 5 patterns. We show here results from 20 hindcasts of recent warm and cold ENSO episodes: the start dates are given in Table 1 and indicated in Fig. 6. (These dates have also been specifically considered by Latif et al., 1993b, 1994; Balmaseda et al., 1994; Wu et al., 1994.) In most of our hindcasts, the initial SST anomalies tend to decay, in some cases after a short period of amplification. In extended integrations, the coupled model did not oscillate freely but tended to a state with warm central Pacific and cool east Pacific SST anomalies with a strong seasonal cycle, giving slightly cool Niño3 SST′ on average.

Fig. 8a–e shows SST′ averaged over the Niño3 area in the equatorial central-east Pacific (5°S–5°N, 150°W–90°W), for the simulation and

Table 1. *Starting times of 20 hindcasts of recent ENSO events*

1972/73 warm	1973/74 cold	1982/83 warm	1986/87 warm	1987/88 cold
1/10/71	1/10/72	1/10/81	1/4/86	1/7/87
1/1/72	1/1/73	1/1/82	1/7/86	1/10/87
1/4/72	1/4/73	1/4/82	1/10/86	1/1/88
1/7/72	1/7/73	1/7/82	1/1/87	1/4/88

the 20 hindcasts. Hindcasts starting before the 1972/73 warm peak initially warmed, but then cooled too soon. The July 1972 and October 1972 hindcasts starting near the peak followed the decline of the event well, but did not capture the succeeding cold phase, while later hindcasts starting in 1973 overestimated the degree of cooling. Hindcasts of the exceptional 1982/83 major warm event, starting from preceding cool conditions, were all unsuccessful, although the first 3 hindcasts

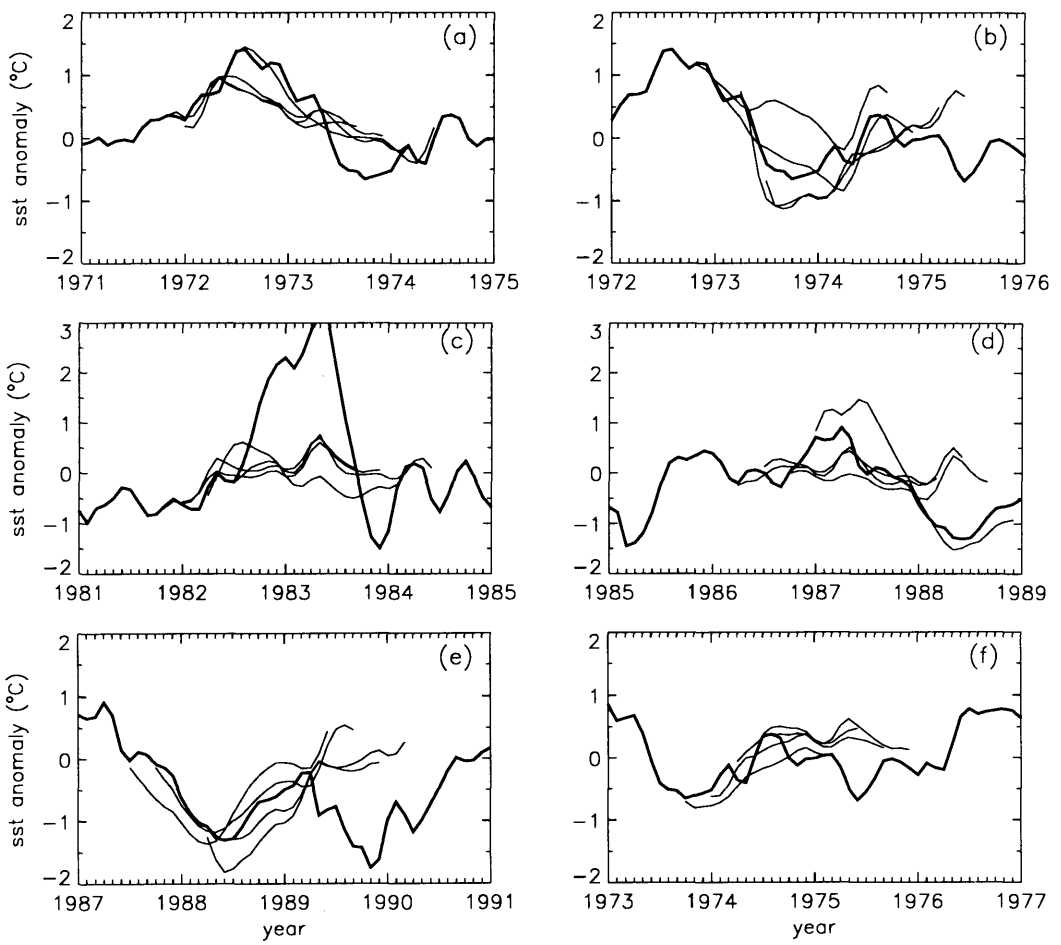

Fig. 8. SST anomalies averaged over the Niño3 area (5° N–5° S, 150° W–90° W) for: (a)–(e) 5 sets of 4 hindcasts for recent warm and cold ENSO episodes; (f) 4 hindcasts of the 74/75 non-event. The thick curve indicates simulated SST anomalies, while hindcasts are thin curves. Hindcasts were made using the ocean GCM coupled to an empirical atmosphere based on 5 SST′ EOFs and associated wind stress anomalies.

Tellus A/46/4-8

in this case did warm for the first few months. This failure to predict the largest event was disappointing, as other models (e.g., Cane et al., 1986; Latif et al., 1993b) have succeeded: note however that the 1982/83 predictions by Barnett et al. (1993) using a statistical atmosphere were only weakly warm. Reasons for this failure are investigated below.

The 1986/87 warm event was weak in the Niño3 region simulation compared to observations (Fig. 3); this event peaked further west in the simulation (Fig. 1) with amplitude like that observed. Initial anomalies in the hindcasts remained very small, except for the January 1987 hindcast which amplified existing warm conditions. The 1987/88 cold event and subsequent recovery was generally well predicted. Overall, hindcasts were best when starting in the transition from warm to cool conditions. Some extra shorter-range hindcasts of the 1974/75 "non-event" (when conditions seemed to favour development of a warm event that did not in fact occur) are given in Fig. 8f: perhaps fortuitously, no event develops in the model. (These extra cases are not included in the analysis below.)

Fig. 9 shows the correlations and rms errors between hindcast and observed Niño3 SST anomalies, as a function of lead time. Results using persistence for the same 20 cases are also included for comparison. Correlations exceed 0.5 up to about 12 months lead, well above persistence values after 5 months, and rms hindcast errors are low compared to persistence. (There are substantial errors at lead time 0 because the simulated SST does not match the observed SST. The hindcast skill could be improved by combining the dynamical and persistence estimates, as described by Fraedrich and Smith 1989.) This assessment of hindcast skill looks promising, but bear in mind that hindcast skill is inflated by choosing ENSO events, and persistence skill is low for ENSO events. (The persistence statistics for a larger sample of hindcasts, with start dates 1/61, 4/61, ..., 10/89, are included in Fig. 9: correlations are larger and errors smaller for the larger sample.) Skill is also likely to be inflated somewhat because the hindcasts are made during the period used to calculate the empirical atmosphere statistics. The skill of POP hindcasts made by continuing the natural cycle of a POP mode is likely to be comparable to that of the dynamical hindcasts (Latif et al., 1993b; Balmaseda et al., 1994; Wu et al., 1994). Other regions were also assessed: hindcast skill was no better than persistence in the west Pacific, but east of the Niño3 region in the equatorial Pacific skill was similar to (but lower than) that for Niño3.

Trajectories of the predictors q_k (which can be

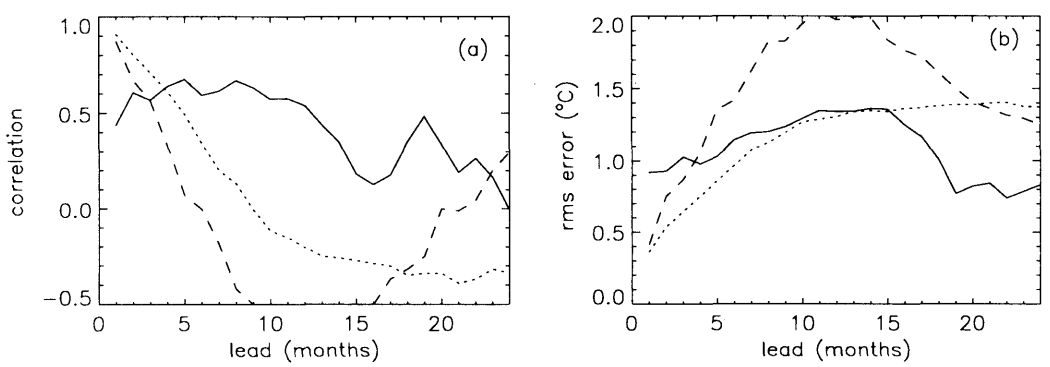

Fig. 9. Statistics of hindcasts of SST anomalies averaged over the Niño3 area (5° N–5° S, 150° W–90° W), as a function of lead time. Model hindcasts were made for 5 sets of 4 hindcasts for recent warm and cold ENSO episodes, using the ocean GCM coupled to an empirical atmosphere based on 5 SST′ EOFs and associated wind stress anomalies. (a) Correlation of observed and model hindcast anomalies (solid), of observed and persisted anomalies for the same 20 cases (dashed), and of observed and persisted anomalies for cases starting 1/61, 4/61, ..., 10/89 (dotted). (b) Root mean square difference between observed and model hindcast anomalies (solid), between observed and persisted anomalies for the same 20 cases (dashed), and between observed and persisted anomalies for cases starting 1/61, 4/61, ..., 10/89 (dotted).

regarded as the coefficients of SST′ eof_k and associated winds), and hindcast errors as a function of initial q_k, were examined to seek reasons for the success or failure of individual hindcasts, and to look for indicators of predictive skill. Not surprisingly, a good hindcast required q_1 to follow the simulated q_1 values closely. (Recall that SST′ eof_1 resembles a peak El Niño pattern and is associated with nearly half of the simulated SST′ variance.) Fig. 10 shows hindcast minus simulated Niño3 SST′ errors for the 20 cases plotted as a function of initial q_1, for a lead time of 12 months. The q_1 amplitudes indicated are for the average of the month preceding a hindcast, as in Fig. 6a: actual initial values differ only slightly. There is no obvious dependence of error on initial q_1, apart from the large 1982/83 errors that tend to be larger for smaller q_1 amplitude. Small initial q_1 does not necessarily imply a poor prediction: the ocean can develop SST anomalies even in the absence of SST (and hence associated wind) anomalies, due to continued evolution of the thermocline shape based on prior wind history. The dependence of model hindcast errors on other factors (other SST patterns, heat content patterns, and initial amplitude of the ENSO-related POP mode) was similarly investigated, but again no clear signal emerged. Such a signal (if it exists!) may be obscured here by the small number of cases considered, or by seasonal effects.

Considering the 1982/83 cases in particular, 3 hindcasts (October 1981, January and April 1982) start with negative q_1, giving easterly stress anomalies. The evolving thermocline shape leads to slight warming of model SST′, but no major warming like that observed develops. To seek reasons for this failure, and to further test the empirical atmosphere, the ocean model was forced with wind stress anomalies reconstructed using SST′ from the simulation for this period. The reconstructed winds (Fig. 7) are somewhat weaker than observed in 1982/83, and a correspondingly weaker 1982/83 warm event was produced, with the late 1982 SST′ peak (Fig. 1) reduced in particular. The warming did not extend to the South American coast, in contrast to the simulation with observed winds. This lack of warming near the South American coast seems to be due to the lower wind strength (and consequent smaller thermocline displacement), rather than a faulty wind pattern, because the reconstruction reproduced the observed eastward shift of westerly wind anomalies adequately. Stress anomalies reconstructed in turn from this new SST′ were similar to those from the first reconstruction, but with the onset of central Pacific westerlies delayed until late 1982. This result suggests that the empirical winds ought to be sufficient to drive a weakened warm event. A possible reason for poor amplification of warming in the coupled model may be that the damping effect of the surface heat flux (which opposes SST′) is too strong in this model.

The tendency for simulated SST′ to peak too far west may be an ocean model defect that also inhibits any major warming: if the model could develop warmer SST′ further east, then corresponding displacement of westerly wind stress anomalies would help to amplify such warming.

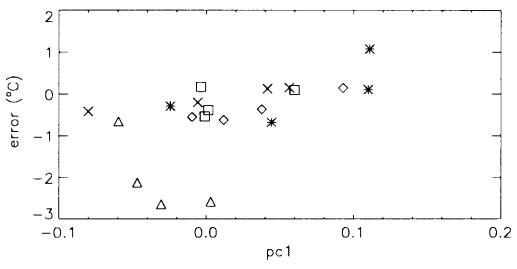

Fig. 10. Error (hindcast minus simulated) of SST′ in the Niño3 region, at a lead time of 12 months, for 20 hindcasts of recent warm and cold ENSO events, as a function of the coefficient pc_1 of SST′ eof_1 in the month preceding each hindcast start date (Fig. 6a). Hindcasts in groups of 4 are denoted ◇ for 1971/72, ∗ for 1972/73, △ for 1982/83, □ for 1986/87, and × for 1987/88.

6. Summary

The development of a model with the objective of predicting sea surface temperatures in the tropical Pacific is described. A high resolution general circulation model of the tropical Pacific ocean is forced with observed wind stresses for the period 1961 to 1993. An empirical atmosphere model is then designed, based on the statistical relationship between the simulated sst anomaly patterns and the observed wind stress anomalies.

When the ocean model is forced with the observed wind stresses it quite realistically

simulates observed interannual variability, and temperature anomalies in most regions are in good agreement with observations. A failing in common with other models is that the SST variability tends to be confined too close to the equator and that the maximum amplitude on the equator is displaced to the west of the observed maximum close to the east coast. The evolution of individual warm and cold phases is not always the same: in particular the 1982/83 event exhibits eastward phase propagation in temperature anomaly while at other times there is little movement, with a weak tendency for westward propagation in the central Pacific. A POP analysis combining SST, heat content and wind stress anomalies has been employed to try to derive a characteristic space/time structure for the simulation. The low frequency ENSO related pattern that emerges is that of an oscillating system involving slow propagation of heat content anomalies. This is consistent with a similar analysis of observed data (Latif et al., 1993b), and equates to the description of the delayed action oscillator (Saurez and Schopf, 1988).

Several hindcasts of cold and warm ENSO episodes were carried out using the ocean general circulation model coupled to the empirical atmosphere. A study of the individual cases shows a range of behaviour: in general the hindcasts are better in the transition from warm to cool conditions. The model does not produce strong warming: in particular, the hindcasts for the 1982/83 event failed. The reasons for this failure are not clear: one possible cause is that the empirical winds are not strong enough to generate SST′ increases that outweigh the damping effect of surface heat fluxes.

Combining information from 20 cases, shows a model skill exceeding the 0.5 correlation level at a lead time of out to 12 months in the central-east Pacific, which is well above persistence values after the first five months. The skill is initially lower than persistence due to errors in the prescribed ocean initial conditions, and an improvement would be expected if observed ocean data were assimilated as part of the initial analysis. In an attempt to achieve a higher skill other methods of building the empirical atmosphere are being tested: a trial hindcast with an empirical atmosphere based on heat content anomalies was made for the 1982/83 ENSO event, with improvement on the poor hindcasts with the SST based atmosphere. Barnett et al. (1993) found that seasonal dependence was an important factor in the performance of their empirical atmosphere, and this aspect is being investigated for the present model. Balmaseda (1993) suggests that improvements can also be made by organising the EOFs into ENSO related modes by POP analysis.

7. Acknowledgements

David Anderson contributed useful ideas, particularly with regard to the statistical atmosphere. Grant Kelly assisted with data management, and James Stricherz of Florida State University kindly provided the wind data. The work was partially supported by the Commission of the European Communities under Contract EPOC-0003-C(MB).

REFERENCES

Balmaseda, M. A. 1993. *Simulacion y prediccion del fenomeno ENSO con un modelo acoplado oceano-atmosfera.* PhD thesis, University of Alcala, Spain.

Balmaseda, M. A., Anderson, D. L. T. and Davey, M. K. 1994. ENSO prediction using a dynamical ocean model coupled to statistical atmospheres. *Tellus* **46**, 000–000.

Barnett, T. P., Graham, N. E., Cane, M. A., Zebiak, S. E., Dolan, S. C., O'Brian, J. J. and Legler, D. M. 1988. On the prediction of the El Niño of 1986–87. *Science* **241**, 192–196.

Barnett, T. P., Latif, M., Graham, N., Flügel, M., Pazan, S. and White, W. 1993. ENSO and ENSO related predictability, Part 1: Prediction of equatorial sea surface temperature with a hybrid coupled ocean-atmosphere model. *J. Clim.* **6**, 1545–1566.

Bengtsson, L., Schlese, U., Roeckner, E., Latif, M., Barnett, T. P. and Graham, N. 1993. A two-tiered

approach to long-range climate forecasting. *Science* **261**, 1026–1029.

Busalacchi, A. J., Takeuchi, K. and O'Brien, J. J. 1983. Interannual variability of the equatorial Pacific revisited. *J. Geophys. Res.* **88**, 7551–7562.

Cane, M. A. and Zebiak, S. E. 1985. A theory for El Niño and the Southern Oscillation. *Science* **228**, 1085–1087.

Cane, M. A., Zebiak, S. E. and Dolan, S. C. 1986. Experimental forecasts of El Niño. *Nature* **321**, 827–832.

Chao, Yi and Philander, S. G. H. 1993. On the structure of the Southern Oscillation. *J. Clim.* **6**, 450–469.

Cox, M. D. 1984. *A primitive equation, 3-dimensional model of the ocean.* GFDL Ocean Group Tech Rep. 1, Geophys. Fluid Dyn. Lab./NOAA, Princeton, NJ, USA.

Esbensen, S. K. and Kushnir, Y. 1981. *The heat budget of the global ocean: an atlas based on estimates from marine surface observations.* Rep. no. 29, Climate Res. Inst., Oregon State University, Corvallis.

Fraedrich, K. and Smith, N. R. 1989. Combining predictive schemes in long-range forecasting. *J. Clim.* **2**, 291–294.

Glantz, M. H., Katz, R. W. and Nicholls, N. 1991. *Teleconnections linking worldwide climate anomalies.* Cambridge Univ. Press, 535 pp.

Goldenberg, S. D. and O'Brien, J. J. 1981. Time and space variability of tropical Pacific wind stress. *Mon. Weath. Rev.* **109**, 1190–1207.

Gordon, C. and Corry, R. 1991. A model simulation of the seasonal cycle in the tropical Pacific Ocean using climatological and modeled surface forcing. *J. Geophys. Res.* **96**, C1, 847–864.

Hasselmann, K. 1988. PIPs and POPs: The reduction of complex dynamical systems using Principal Interaction and Oscillation Patterns. *J. Geophys. Res.* **93** (D9), 11015–11021.

Hellerman, S. and Rosenstein, M. 1983. Normal monthly windstress over the world ocean with error estimates. *J. Phys. Oceanog.* **13**, 1093–1104.

Jaeger, L. 1976. Monthly maps of precipitation for the world ocean. *D. Wetterd. Ber.* **18**, no. 139.

Kraus, E. B. and Turner, J. S. 1967. A one-dimensional model of the seasonal thermocline. Part II. *Tellus* **19**, 98–105.

Kubota, M. and O'Brien, J. J. 1988. Variability of the upper tropical Pacific ocean model. *J. Geophys. Res.* **93**, 13930–13940.

Latif, M., Barnett, T. P., Cane, M. A., Flügel, M., Graham, N. E., Von Storch, H., Xu, J.-S. and Zebiak, S. E. 1994. A review on ENSO prediction studies. *Climate Dyn.* **9**, 167–179.

Latif, M., Sterl, A., Maier-Reimer, E. and Junge, M. M. 1993a. Climate variability in a coupled GCM. Part 1: the tropical Pacific. *J. Clim.* **6**, 5–21.

Latif, M., Sterl, A., Maier-Reimer, E. and Junge, M. M. 1993b. Structure and predictability of the El Niño/Southern Oscillation phenomenon in a coupled ocean-atmosphere general circulation model. *J. Clim.* **6**, 700–708.

Levitus, S. 1982. *Climatological atlas of the world ocean.* NOAA Prof. Paper No. 13.

Miller, A. J., Barnett, T. P. and Graham, N. E. 1993. A comparison of some tropical ocean models: hindcast skill and El Niño evolution. *J. Phys. Oceanog.* **23**, 1567–1591.

Miyakoda, K., Rosati, A. and Gudgel, R. 1993. *Toward the GCM El Niño simulation.* NATO ASI Series, vol. 16, 125–151.

Oberhuber, J. M. 1988. *An atlas based on the COADS dataset.* Max-Planck-Institut für Meteorologie Report no. 15.

Pacanowski, R. and Philander, S. G. H. 1981. Parametrization of vertical mixing in numerical models of the tropical oceans. *J. Phys. Oceanog.* **11**, 1443–1451.

Philander, S. G. H., Pacanowski, R., Lau, N.-C. and Nath, M. J. 1992. Simulation of ENSO with a global atmospheric GCM coupled to a high resolution tropical Pacific Ocean model. *J. Clim.* **5**, 308–329.

Seager, R. 1989. Modeling tropical Pacific sea surface temperature: 1970–1987. *J. Phys. Oceanog.* **19**, 419–434.

Stockdale, T. 1992. *Simulation and prediction of tropical SST with a coupled ocean-atmosphere model.* DPhil thesis, Oxford University, UK.

Stockdale, T., Anderson, D., Davey, M., Delecluse, P., Kattenberg, A., Kitamura, Y., Latif, M. and Yamagata, T. 1993. *Intercomparison of tropical ocean GCMs.* WCRP-79, WMO/TD-No. 545, 90 pp.

Suarez, M. J. and Schopf, P. S. 1988. A delayed action oscillator for ENSO. *J. Atmos. Sci.* **45**, 3283–3287.

Von Storch, H., Bürger, G., Schnur, R. and Von Storch, J.-S. 1993. *Principal oscillation patterns.* Max-Planck-Institut für Meteorologie Report no. 113.

Wakata, Y. and Sarachik, E. S. 1991. On the role of equatorial ocean modes in the ENSO cycle. *J. Phys. Oceanog.* **21**, 434–443.

Wells, N. C. and King-Hele, S. 1990. Parameterization of tropical ocean heat flux. *Q. J. Roy. Met. Soc.* **116**, 1213–1224.

Wu, D.-H., Anderson, D. L. T. and Davey, M. K. 1993. ENSO variability and external impacts. *J. Clim.* **6**, 1703–1717.

Wu, D.-H., Anderson, D. L. T. and Davey, M. K. 1994. ENSO prediction experiments using a simple ocean-atmosphere model. *Tellus* **46A**, 465–480.

Xu, J.-S. and Von Storch, H. 1990. Principal oscillation patterns-prediction of the state of ENSO. *J. Clim.* **3**, 1316–1329.

Zebiak, S. E. 1989. Oceanic heat content variability and El Niño cycles. *J. Phys. Oceanog.* **19**, 475–486.

Zebiak, S. E. and Cane, M. A. 1987. A model El Niño, Southern Oscillation. *Mon. Weath. Rev.* **115**, 2262–2278.